

A Method to Extrapolate the Diffuse Upwelling Radiance Attenuation Coefficient to the Surface as Applied to the Marine Optical Buoy (MOBY)

KENNETH J. VOSS AND HOWARD R. GORDON

Physics Department, University of Miami, Coral Gables, Florida

STEPHANIE FLORA

Moss Landing Marine Laboratory, San Jose State University, Moss Landing, California

B. CAROL JOHNSON

Sensor Science Division, National Institute of Standards and Technology, Gaithersburg, Maryland

MARK YARBROUGH, MICHAEL FEINHOLZ, AND TERRENCE HOULIHAN

Moss Landing Marine Laboratory, San Jose State University, Moss Landing, California

(Manuscript received 5 December 2016, in final form 7 April 2017)

ABSTRACT

The upwelling radiance attenuation coefficient K_{Lu} in the upper 10 m of the water column can be significantly influenced by inelastic scattering processes and thus will vary even with homogeneous water properties. The Marine Optical Buoy (MOBY), the primary vicarious calibration site for many ocean color sensors, makes measurements of the upwelling radiance L_u at 1, 5, and 9 m, and uses these values to determine K_{Lu} and to propagate the upwelling radiance directed toward the zenith, L_u , at 1 m to and through the surface. Inelastic scattering causes the K_{Lu} derived from the measurements to be an underestimate of the true K_{Lu} from 1 m to the surface at wavelengths greater than 575 nm; thus, the derived water-leaving radiance is underestimated at wavelengths longer than 575 nm. A method to correct this K_{Lu} , based on a model of the upwelling radiance including Raman scattering and chlorophyll fluorescence, has been developed that corrects this bias. The model has been experimentally validated, and this technique can be applied to the MOBY dataset to provide new, more accurate products at these wavelengths. When applied to a 4-month MOBY deployment, the corrected water-leaving radiance L_w can increase by 5% (600 nm), 10% (650 nm), and 50% (700 nm). This method will be used to provide additional and more accurate products in the MOBY dataset.

1. Introduction

The Marine Optical Buoy (MOBY) (Clark et al. 1997, 2003) has been the primary vicarious calibration site for many—if not all—ocean color satellite instruments since 1997 (Barnes et al. 2001; Eplee et al. 2001; Franz et al. 2007; Wang et al. 2013). This dataset provides the water-leaving spectral radiance $L_w(\lambda)$ and normalized water-leaving radiance $L_{wn}(\lambda)$ to satellite programs for use in the vicarious calibration process (Clark et al. 1997), and as such is required to provide these parameters with the highest possible accuracy. MOBY has three arms—at 1-, 5-, and 9-m

depths—for measuring the upwelling radiance $L_u(\lambda, z)$, so the shallowest depth that MOBY measures L_u is at 1 m. To propagate this measurement to the surface requires an estimate of $K_{Lu}(\lambda, 0, 1)$, the diffuse upwelling radiance attenuation coefficient for the depths from 0 to 1 m (referred to as K01 for simplicity). The diffuse attenuation coefficient between depths z_1 and z_2 is defined as

$$K_{Lu}(\lambda, z_1, z_2) = -\frac{\ln \left[\frac{L_u(\lambda, z_2)}{L_u(\lambda, z_1)} \right]}{z_2 - z_1}. \quad (1)$$

Also needed are the transmission of the air–sea interface for upwelling radiance, and the index of

Corresponding author: Kenneth Voss, voss@physics.miami.edu

DOI: 10.1175/JTECH-D-16-0235.1

© 2017 American Meteorological Society. For information regarding reuse of this content and general copyright information, consult the [AMS Copyright Policy](#) (www.ametsoc.org/PUBSReuseLicenses).

refraction of the water to account for refractive effects on the radiance due to the air–sea interface. These latter two parameters are assumed to be constant but K01 is variable and must be determined for each dataset.

The current estimate of K01 is derived by using this upper arm measurement at 1 m, combined with either the measurement of $L_u(\lambda, z)$ at 5 or 9 m. In general, the pair of measurements at 1 and 5 m are used to form $K_{Lu}(\lambda, 1\text{ m}, 5\text{ m})$ (K15), and this is assumed to represent K01. For the MOBY products named L_w1 and $L_{wn}1$, $L_u(\lambda, 1\text{ m})$ is propagated to the surface using K15. In the clear water where MOBY is located, for wavelengths greater than 575 nm $K_{Lu}(\lambda)$ is not constant with depth due to Raman scattering (Sugihara et al. 1984) and chlorophyll fluorescence (Gordon 1979). In general, for these wavelengths K15 will be less than K01 due to the increasing fraction of light that has been inelastically scattered from the blue region of the spectrum, where energy is abundant, to the red region, where the incoming light is rapidly attenuated. It has been pointed out that using K15 in place of K01 in the region above 575 nm causes the $L_w(\lambda)$ and $L_{wn}(\lambda)$ derived from MOBY to be underestimated by approximately 20% at 700 nm of their true values (Li et al. 2016). This paper will describe a method to estimate the correct K01 using a validated model of K01 in terms of K15 and K19 along with the measured K15 and K19.

2. Model and validation

As described above, the goal is to develop a model for estimating K01 given K15, K19, or K59, or some combination of these. The model is derived by simulating the in-water light field utilizing radiative transfer computations.

The site where MOBY is located, off of the island of Lanai, Hawaii, can be considered case 1 waters over 90% of the time (using the criteria of Lee and Hu 2006), meaning that the inherent optical properties (absorption and scattering coefficients, etc.) covary with the concentration of chlorophyll-*a* (Chl) (Morel and Prieur 1977), and can be modeled using the single parameter Chl. At the site, the range of Chl is also quite limited and is between 0.05 and 0.15 mg m⁻³ over 98% of the time. In addition, since the MOBY measurements are made for the specific purpose of vicarious calibration of polar-orbiting ocean color satellites, the measurements are usually performed within 3 h of solar noon, which results in a somewhat limited range of solar zenith angles in this location (less than 55°). Thus, the parameter space that must be filled with model results is limited. With these constraints, a Monte

Carlo radiative transfer model, including Raman inelastic scattering, was used to determine K01, K15, K05, K59, and K19 for four values of Chl (0, 0.05, 0.10, 0.15 mg m⁻³), six solar zenith angles (SZA = 10°, 20°, 30°, 40°, 50°, and 60°), and for every 10 nm from 400 to 700 nm.

The Monte Carlo code used in this study is described in detail in Gordon (1999). The code can operate in two modes. In the first mode, attention is focused on elastic scattering, and even though losses due to Raman scattering are included, only the elastically scattered light field is computed. In the second mode, interest is centered on the inelastically scattered (Raman) light field. In this case, photons are started at the Raman excitation wavelength and elastically scattered in the medium, but, unlike the first mode, this time when a Raman scattering takes place, that photon is followed in detail, allowing computation of the Raman-generated light field. Thus, for a given wavelength of interest, the code is run twice: once in the elastic scattering mode (first mode) at the wavelength of interest to generate the elastic portion of the light field and once in the second mode (in which photons enter the top of the atmosphere at the appropriate excitation wavelength for the wavelength of interest) to generate the Raman portion of the light field. These two calculations are then combined to generate the total light field. The inherent optical properties of the water and particles are similar to those in Gordon (1999), but they have been tuned to provide radiances in better agreement with actual measurements at the MOBY site for wavelengths from 400 to 600 nm.

As expected, the results from this Monte Carlo model show that K_{Lu} depends on the pair of depths used, Chl, and the solar zenith angle. Figure 1 shows the Monte Carlo results for three different Chl values for K01 as a function of wavelength at 10° SZA. Also shown are K15/K01, K59/K01, and K19/K01 for the three Chl values. For wavelengths less than 575 nm, K01 is the same as K15 and K19 to within 3%. Above 575 nm, the K_{Lu} values rapidly diverge. The effect of using one of these K_{Lu} values to provide K01 would be to underestimate L_w or L_{wn} in this spectral region. Above 700 nm the values would continue to diverge, but because of issues such as instrument self-shadowing (Gordon and Ding 1992; Mueller 2004) and very small L_w , MOBY data above 700 nm are not used for vicarious calibration and will not be discussed in this paper.

Other features to note in Fig. 1 are that the best approximation for K01 is K15 followed by K19. K59 deviates the most from K01. When an error analysis is carried out on the various environmental effects that

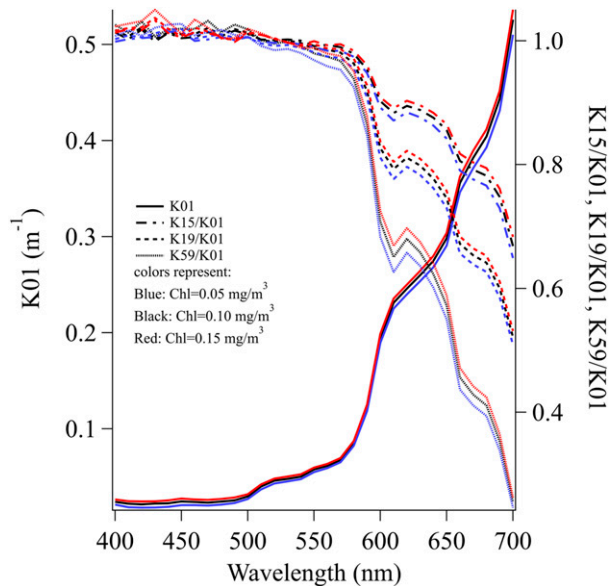


FIG. 1. Modeled K_{01} (left axis) and the modeled ratios K_{15}/K_{01} , K_{19}/K_{01} and K_{59}/K_{01} (right axis) for $\text{Chl} = 0.05 \text{ mg m}^{-3}$ (blue), $\text{Chl} = 0.10 \text{ mg m}^{-3}$ (black), and $\text{Chl} = 0.15 \text{ mg m}^{-3}$ (red), all at 10° SZA.

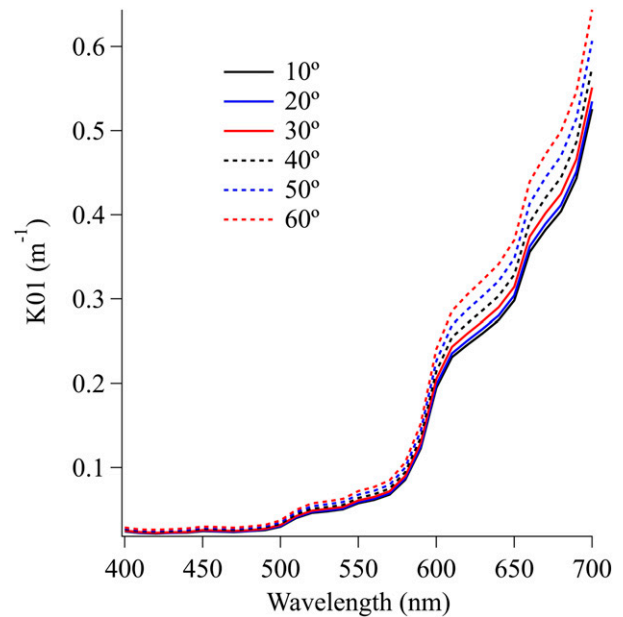


FIG. 2. Variation in modeled K_{01} with wavelength and SZA, with $\text{Chl} = 0.1 \text{ mg m}^{-3}$.

can interfere with the calculation of $K_{Lu}(\lambda)$, K19 has the least uncertainty (excluding inelastic effects) because it spans a larger depth range. Thus, we will concentrate on the relationship between K15 (because it is the closest to K01) and K19 (because it theoretically should have the least uncertainty), and we will not discuss K59 until the [appendix](#).

$K_{Lu}(\lambda)$ also depends on the solar zenith angle. [Fig. 2](#) shows the variation of the modeled K_{01} with SZA and Chl is 0.10 mg m^{-3} . As expected, particularly for wavelengths above 600 nm, there is a stronger dependence on solar zenith angle at angles greater than 30° than on Chl , for the range of Chl expected at the MOBY site. Fortunately, for any specific measurement the solar zenith angle is known, so an appropriate set of K_{Lu} values can easily be determined.

The accuracy of the model results primarily depends on the input to the model. This radiative transfer model has been shown to agree precisely with other radiative transfer models when given the same input optical properties and boundary conditions ([Mobley et al. 1993](#)). Thus, the accuracy of the model results depends on the input parameters, which depend, in this case, on the suitability of the parameters used in the model to represent measurements in the field. To validate these model results, we used a dataset of hyperspectral $L_u(\lambda, z)$ measurements performed in the Hawaiian Islands ([Yarbrough et al. 2007a](#)). It is difficult to make measurements both near the surface

and in the region above 600 nm, where instrument self-shading is a large factor due to the high absorption of water itself. A specialized instrument was developed to operate in this spectral region, which was based on a remotely operated vehicle (ROV) with a fiber-optic collector extending a meter in front of the ROV ([Yarbrough et al. 2007b](#)). The fiber extended from the ROV to the ship, where it was coupled to a spectrometer with 1-nm resolution from 350 to 900 nm. The ROV was placed at several different depths, so profiles of the near-surface water column could be obtained. A subset of data from this experiment was selected to validate these model results. We selected profiles that were in deep water, had measurement depths within 10 cm of the surface paired with measurements at 1- and 5-m depths (but often there was also a measurement at 9-m depth), and were performed in a reasonably short period of time (1 h). Two effects can happen over this short time: first, the incident light field can change; second, the geometry of the in-water light field can change. The first effect, while it can be large, is negated by normalizing to simultaneous measurements of the hyperspectral incident irradiance field, as was done. The second effect can be explored using the model of [Morel et al. \(2002\)](#), for nadir view, as a function of solar zenith angle. For sun angle changes that occur within 1 h, the radiance changes that occur due to this factor would cause less than a 1% uncertainty in K_{Lu} . As part of the criteria, the K_{Lu} values derived from the measurement pairs

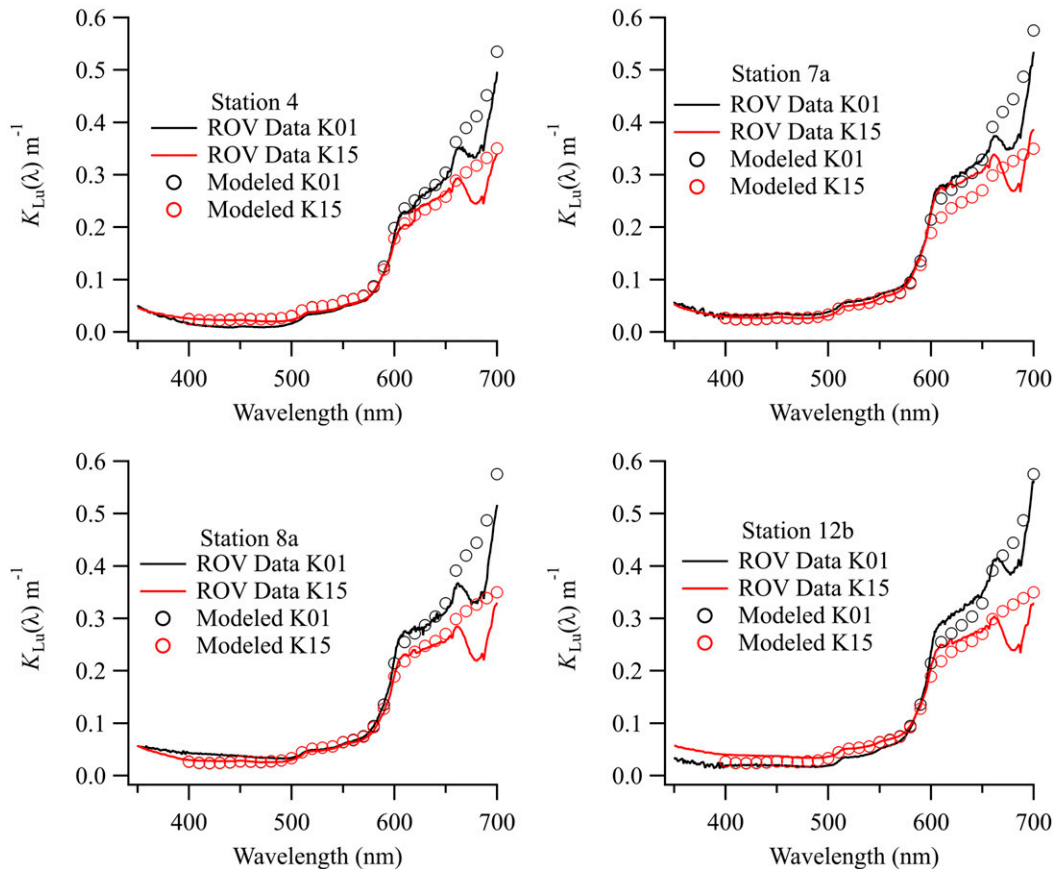


FIG. 3. Comparison of modeled and ROV data for several deep-water stations during a cruise off of Oahu, Hawaii, during the period 22 Oct–5 Nov 2003. Model data were interpolated to the appropriate SZA for that dataset, but assumed a constant Chl value of 0.10 mg m^{-3} . Note in these graphs, the effect of Chl fluorescence has not been included in the model results.

had to agree to within 0.03 m^{-1} for the wavelength range from 400 to 550 nm. In general the data typically either passed this last criteria easily or the difference between the K_{Lu} values derived from the measurement pairs was very large ($>0.05 \text{ m}^{-1}$), indicating the data could not be normalized properly by surface irradiance during the time of the profile.

Figure 3 shows the comparison between the model and ROV data for four representative datasets. The model results here assume a Chl value of 0.10 mg m^{-3} , and the model results are linearly interpolated to match the SZA of the data. The figure shows that the model represents the measured K15 and K01 reasonably well except for the region between 660 and 700 nm, where chlorophyll fluorescence (which was not included in the original model) is important. Making a model that includes this fluorescence from first principles is difficult because, as opposed to Raman, which depends on the physical properties of water (Bartlett et al. 1998), chlorophyll fluorescence

depends not only on the amount of chlorophyll in the water, but also on the physiological status of the phytoplankton containing the chlorophyll (Kiefer 1973). The light history, packaging, and many other factors can affect the quantum efficiency of fluorescence η and thus the depth of the feature, or “Dip,” in K_{Lu} . However, with our dataset from the ROV data, we could investigate the possibility of an empirical method to include this Dip in our K_{Lu} .

To investigate the Dip in K_{Lu} , we went back to our ROV dataset and relaxed the selection criteria to include more data. In this case we, allowed measurements that varied less than 0.1 m^{-1} in the region between 400 and 550 nm and, additionally, required that $K_{Lu} < 1 \text{ m}^{-1}$ between 660 and 700 nm. This had the effect of excluding data that had larger variations of surface irradiance during measurement than we could handle with the typical downwelling sky irradiance (E_s) normalization procedures. We then formed a baseline using measurements at 660 and

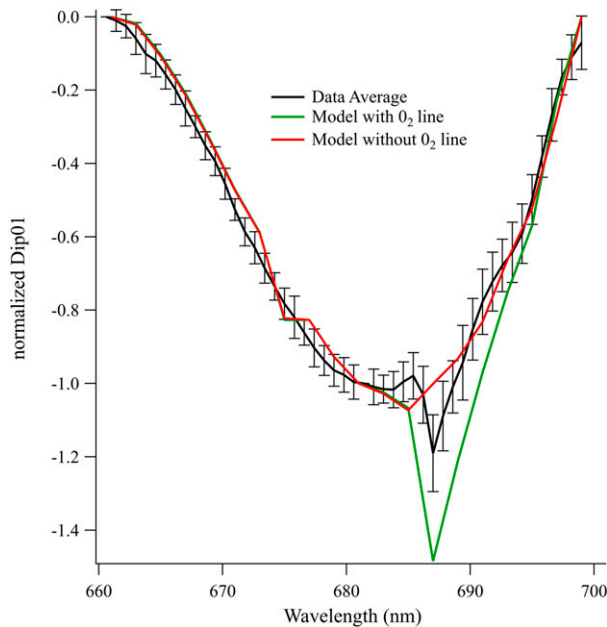


FIG. 4. Deviation of K_{Lu} from a straight baseline between 660 and 700 nm, due to Chl fluorescence and an atmospheric oxygen absorption band at 687 nm. Shown are the average of the data, normalized to the value at 681 nm, and the standard deviation of this average. Also shown are the model results with and without the oxygen band. In the model $Chl = 0.1 \text{ mg m}^{-3}$, $SZA = 10^\circ$, and $\eta = 0.45\%$.

700 nm, and found the difference between this baseline and the measured K_{Lu} for each K_{Lu} (K01, K15, K19, and K59). Each dataset was then normalized to the value at 681 nm, to derive an overall shape for the Dip. The average shape and standard deviation are shown in Fig. 4. The sharp feature in the data at 687 nm is caused by an atmospheric oxygen absorption band at this wavelength, and the associated line filling, similar to Fraunhofer line filling (Ge et al. 1995). This is illustrated by including the results of modeling this chlorophyll Dip with and without the oxygen feature, as shown in Fig. 4. In this figure the model assumed a typical value for that location ($Chl = 0.1 \text{ mg m}^{-3}$, $SZA = 10^\circ$, and $\eta = 0.45\%$). What can be seen, however, is that the average of the data is a very good representation of the shape of the Dip (the standard deviation is small) and we use this average to develop our correction to K01 for this feature.

To handle the variation of the Dip with the physiological parameters of the phytoplankton, we investigated the data and found there was a consistent relationship between the magnitude of the Dip at 681 nm (determined with the baseline at 660 and 700 nm) in K15 (Dip15) and K19 (Dip19) as shown in Fig. 5. We also found that while there was a relationship

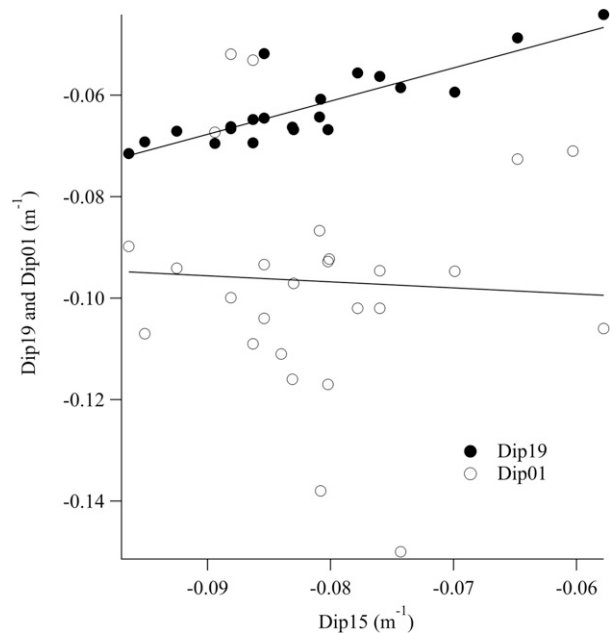


FIG. 5. Dip19 and Dip01 vs Dip15 (all values for the Dip at 681 nm). Lines are a linear least squares fit to the data. As can be seen, Dip15 and Dip19 have a relationship with each other ($r^2 = 0.69$), while Dip01 and Dip15 have no significant relationship ($r^2 = 0.003$).

between Dip15 and Dip19 ($r^2 = 0.69$), there was not a relationship between either Dip15 and Dip01 ($r^2 = 0.003$) or between Dip19 and Dip01 ($r^2 = 0.019$). There was also not a relationship between Dip05 and Dip59. There was also no dependence of Dip01 with Chl or incident irradiance (although all the data, as with MOBY data, were collected within 2 h of solar noon). Thus, we were forced to assume a constant value of $-0.10 \text{ m}^{-1} \pm 0.02 \text{ m}^{-1}$ for the Dip01 at 681 nm. Here and throughout this paper the uncertainty is stated as one standard deviation.

3. Correction algorithm

We now have validated all of the steps necessary to form a correction algorithm for the inelastic effects. The steps in the correction algorithm for each dataset are as follows:

- 1) Linearly interpolate the model K_{Lu} tables to get the correct model K_{Lu} values for the specific solar zenith angle of that dataset. The model was also interpolated to the MOBY wavelengths using a piecewise cubic spline interpolation.
- 2) Use the solar zenith–interpolated tables to find which Chl (used as an index) forms the best match between measured and modeled K15 and K19 at 500 nm.

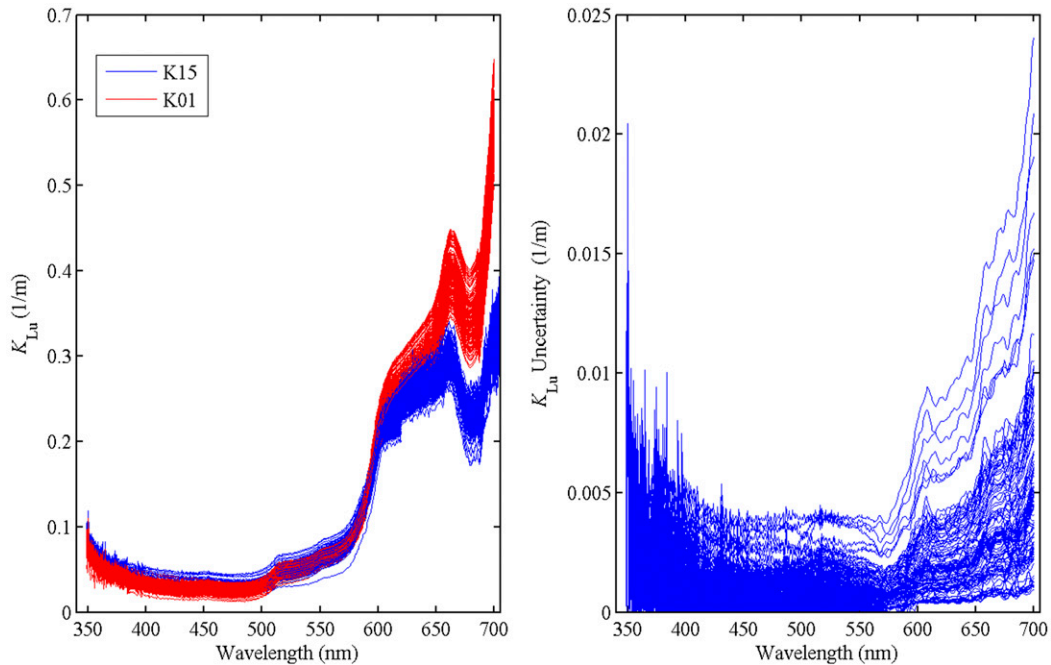


FIG. 6. Modeled $K01_{final}$ and the original K15 for a full MOBY deployment (M253). (left) Values of K_{Lu} , and (right) our estimated uncertainty in $K01_{final}$ associated with the correction procedure.

- 3) Add the average Dip01 scaled by -0.10 m^{-1} at 681 nm.
- 4) Below 500 nm $K01_{final}$ is the measured value K15.
- 5) Above 575 nm $K01_{final}$ is the modeled K01.
- 6) Because the measured K15 is a very good representation of K01 in the region below 575 nm (see Fig. 1),

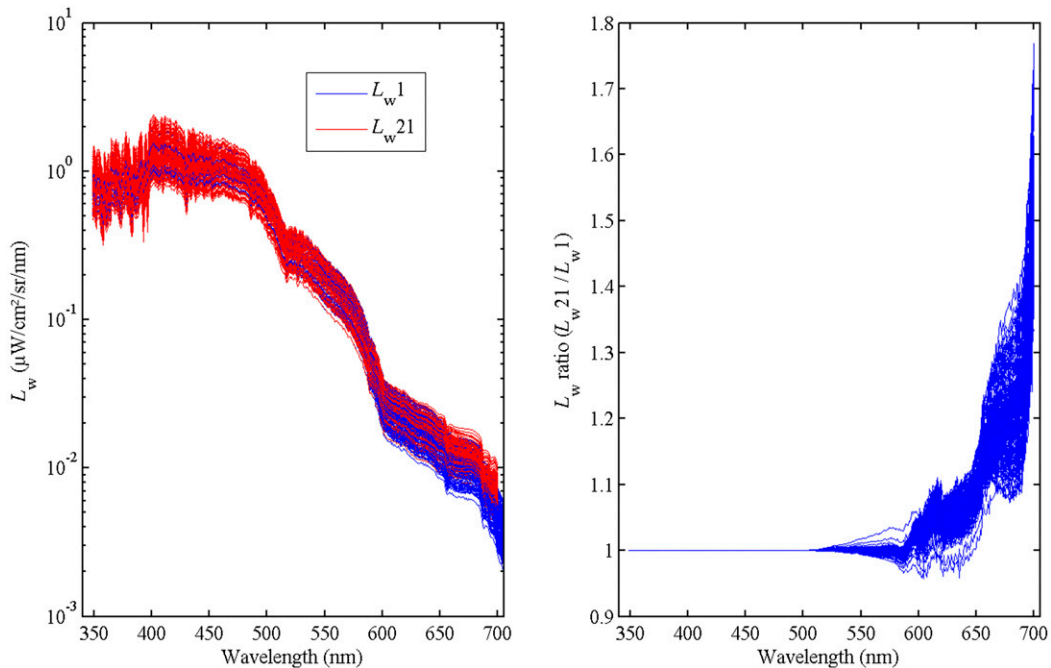


FIG. 7. Effect of using $K01_{final}$ rather than K15 on the retrieved L_w . Values of (left) L_{w1} and L_{w21} , and (right) L_{w21} / L_{w1} . There is no effect below 550 nm, above which the difference grows to 50%.

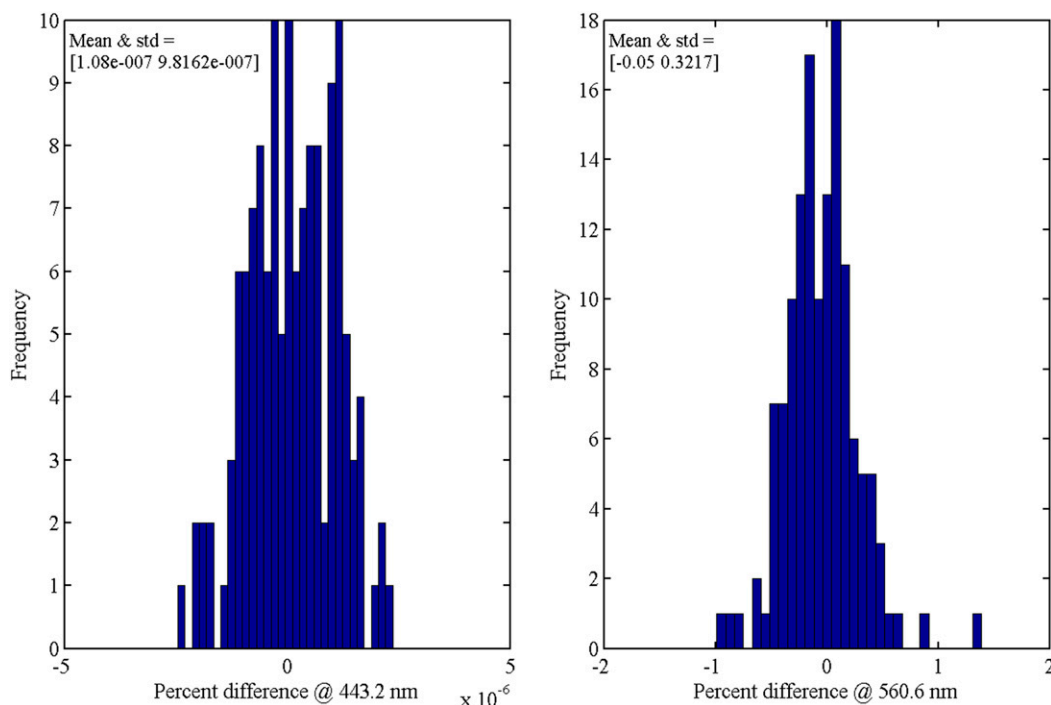


FIG. 8. Histograms of the $100*(L_w21 - L_w1)/L_w21$ for two bands of the *Sentinel-3A* OLCI sensor. These are the 443- and 560-nm bands. Mean and standard deviation of the change can be seen in the upper-left corner of the figures. As can be seen and as expected, there is a negligible change to L_w1 in these wavelengths.

the modeled K01 is blended into the measured K15 over the region from 500 to 575 nm using the equation

$$K01_{final}(\lambda) = \frac{(\lambda - 500 \text{ nm})}{75 \text{ nm}} K01 + \frac{(575 \text{ nm} - \lambda)}{75 \text{ nm}} K15. \tag{2}$$

This $K01_{final}$ can then be used in the data reduction process to propagate $L_u(\lambda, 1 \text{ m})$ to the surface to find $L_w(\lambda)$ and $L_{wn}(\lambda)$. Along with this, we can get an estimate of the uncertainty in this value if we look at the differences between the correction predicted from the two measured K_{Lu} values. Note that this uncertainty reflects only the uncertainty introduced by this process, and not the uncertainty in the fundamental values of K15 and K19. For the region below 500 nm, the uncertainty in the K_{Lu} correction can be obtained by the difference in the measured K15 and K19. Following section 4.3.6 in JCGM (2008), we estimate the uncertainty below 500 nm to be

$$\frac{(K15 - K19)}{2}. \tag{3}$$

Above 575 nm this uncertainty is given by

$$\frac{|K01(K15) - K01(K19)|}{2}, \tag{4}$$

where $K01(K15)$ refers to the K01 derived from the Chl found in the K15 measurement and $K01(K19)$ refers to the K01 derived from the Chl found in the K19 measurement. The region between 500 and 575 nm blends these two values, as in Eq. (2).

To show the effect this has on a set of MOBY data, Fig. 6 shows the original K_{Lu} used to propagate the $L_u(\lambda, 1 \text{ m})$ to the surface, along with the new modeled $K01_{final}$. In addition, it shows the results of the uncertainty calculation as described above. For most of the spectra, as expected, $K01_{final}$ has not changed. However, above 550 nm it starts to depart and rapidly becomes much larger than the original K_{Lu} . The uncertainty meanwhile is much less than 0.01 m^{-1} through much of the spectrum, but it increases in the red wavelengths to be on the order of $0.01\text{--}0.02 \text{ m}^{-1}$, much smaller than the difference between the original and modeled K_{Lu} values.

Figure 7 shows the effect of this change on the calculated L_w , which we call L_w21 to differentiate it from the heritage L_w1 . The major effect is in the red wavelengths, where L_w is very small in either case. As can be seen in the right panel of Fig. 7, while there is no change

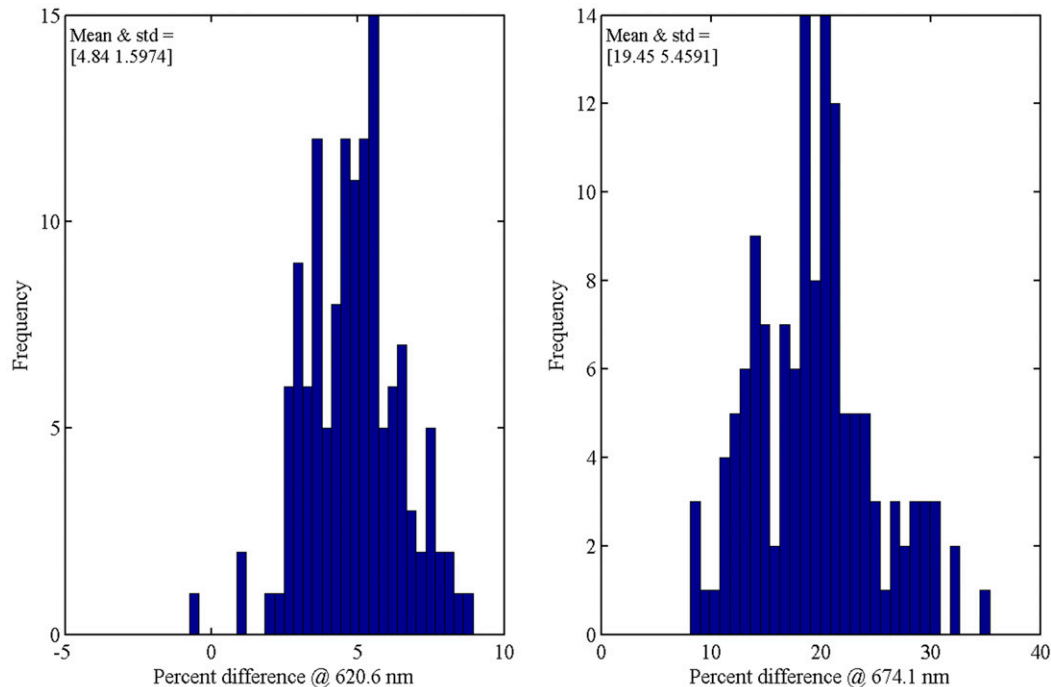


FIG. 9. As in Fig. 8, but for the *Sentinel-3A* OLCI channels at 620 and 674 nm. As the wavelengths get longer, the effect of this change grows due to the correction for the Raman scattering and Chl fluorescence.

below 550 nm, the percent difference between the old and new L_w values grows to be on the order of 50% by 700 nm. For the region between 600 and 700 nm, this correction makes a significant difference to the data.

Figures 8 and 9 show the effect of using $K01_{\text{final}}$ in the calculation of L_w when averaged over several bands of the *Sentinel-3A* Ocean and Land Colour Instrument (OLCI) (Donlon et al. 2012). This sensor was chosen because it is the most recently launched ocean color satellite instrument, and it has several bands between 600 and 700 nm. In Fig. 8, there is little to no effect in the blue and green wavelengths as would be expected. However, Fig. 9 shows that there is a significant difference for the channels between 600 and 700 nm due to the correction for Raman scattering and Chl fluorescence. This change is much larger than our uncertainty of the correction, and it shows that this correction reduces a significant bias in the MOBY dataset at these wavelengths.

4. Conclusions

We have shown that there is a significant bias in the MOBY L_w and L_{wn} dataset for wavelengths above 575 nm due to the influence of Raman scattering and Chl fluorescence in the estimation of K_{Lu} . With a validated model, we can use the existing measurements of K15 and K19 to adjust the model for K01 for each dataset. We can

also use this to estimate the uncertainty in the K01 used to propagate $L_u(\lambda, 1 \text{ m})$ to the surface to produce $L_w(L_w21)$ and $L_{wn}(L_{wn}21)$ for satellite vicarious calibration.

While we have concentrated this work on illustrating the effect and developing a correction algorithm specifically for the MOBY sensor, this work may be generalized in that all in-water measurements must account for this nonlinear K_{Lu} near the surface for wavelengths greater than approximately 575 nm. This is applicable to systems that have both fixed measurement depths and profiling systems. It is obvious from this work that for fixed measurement depth systems, such as MOBY, models must be used to correct the data. Note that for a similar system, Bouée pour l'acquisition de Séries Optiques à Long Terme (BOUSSOLE), the modeled L_w includes the effect of Raman but not Chl fluorescence (Antoine et al. 2008). It is important to note, however, that for profiling systems, the effect of Raman scattering must also be taken into account. Seldom in real-world situations can accurate measurements of the upwelling radiance be made in the upper 1 m of the water column. Most often, to reduce noise the measurements in the upper 3 m of the water column of a profile are accumulated to extrapolate the measurements to the upwelling radiance just below the surface (Zibordi et al. 2011). This extrapolation is commonly done assuming a logarithmic decay of the radiance with depth, which is

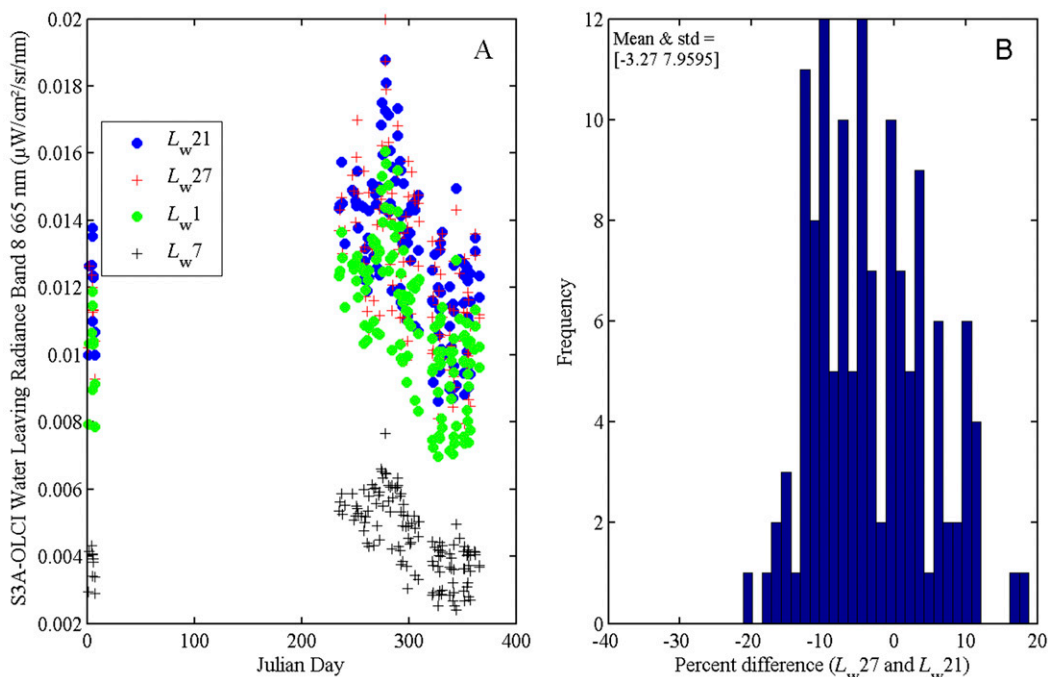


FIG. A1. (a) Value of L_w (665 nm) resulting from the different processing procedures, as described in the text, for a recent MOBY deployment that had all three arms operational for 665 nm. Value of L_w1 is significantly different from that of L_w7 , L_w21 , and L_w27 ; however, the two new processing procedures (L_w21 and L_w27) agree quite closely. This is shown quantitatively in (b) where a histogram of the percent difference between L_w21 and L_w27 is presented. Bias between these products (-3%) and standard deviation (8%) are shown.

similar to assuming that the K_{Lu} is constant with depth. As has been shown, this is not the case at these longer wavelengths and either modeling must be done to extrapolate the measurements to the surface or, at the least, the extrapolation must be done allowing for a nonlinear decay of the log-transformed radiance with depth.

Acknowledgments. This work was supported by NOAA under Grant NA15OAR4320064 and by NASA under Grants NNX14AP63G and NNH11AQ891.

APPENDIX

Algorithm for Additional Products

The preferred MOBY data product for vicarious calibration of ocean color satellites is the L_w1 or L_{wn1} product. As discussed earlier, this product uses $L_u(\lambda, 1\text{ m})$ and K15 to generate $L_u(\lambda, 0-)$, the upwelling radiance just below the sea surface, which is then transmitted through the surface to form L_w1 or L_{wn1} , the latter after normalization by the downwelling surface irradiance.

While MOBY has three measurement depths, at times the measurements from one of the arms are not available, limiting the options for deriving L_w or K_{Lu} . When the 5-m arm is unavailable, we must use K19 to propagate $L_u(\lambda, 1\text{ m})$

to the surface and this product is named L_w2 (or L_{wn2}). In this case the technique described in the text can be used, but the estimation of K01 must depend only on K19 and will be called L_w22 (or L_{wn22}) to differentiate it from L_w21 . This does not have a large effect on the processing, as in general the K01 predicted from K15 and K19 agree quite well. Unfortunately, it is more often the case that if an arm is not available, it is the upper arm that is missing, typically due to a boat striking the buoy. In this case one is left with K59 and propagating $L_u(\lambda, 5\text{ m})$ to the surface to form $L_u(\lambda, 0-)$; this product is called L_w7 and L_{wn7} . As was shown in Fig. 1, K59 is affected much more strongly than K15 or K19 by inelastic processes, and the propagation to the surface of $L_u(\lambda, 5\text{ m})$ is very sensitive to the K_{Lu} used. In addition, we are not modeling K01, but rather K05. However, we can still generate an algorithm that can improve our L_w7 and L_{wn7} product.

In this variation of the algorithm we use K59 to generate a model K05, in a manner similar to the method described earlier. The Dip05, derived from an average of experimental data, as before, has a magnitude of $0.085\text{ m}^{-1} \pm 0.009\text{ m}^{-1}$ at 681 nm. To generate the uncertainty for this new product (called L_w27 or L_{wn27}), we can look at how well L_w27 agrees with these other products when we have all three arms available. A similar situation occurs if we are missing either the 5- or 9-m

measurement; the uncertainties have to be based on how well the final products statistically agree with each other when all three arms are available. Figure A1a shows a comparison between four products— L_w1 , L_w7 , L_w21 , and L_w27 —for band 8 (665 nm) on the Sentinel-3 OLCI sensor. These products were generated for a recent MOBY deployment (M253) for which all arms were operational. The OLCI sensor is chosen as an example because it has several bands in the wavelength range between 600 and 700 nm. As can be seen, the heritage products L_w1 and L_w7 are significantly different from L_w21 and L_w27 ; however, the L_w21 and L_w27 agree with each other quite closely. To see this agreement more quantitatively, Fig. A1b shows a histogram of the percent difference between L_w21 and L_w27 . There is a bias of only -3% (with a standard deviation of 8%) between these two products. This can be compared to the 20% bias between L_w21 and L_w1 , and the 186% bias between L_w27 and L_w7 . Note that L_w27 is a significant improvement over L_w7 and is a good substitute for L_w21 when the top arm is unavailable.

REFERENCES

- Antoine, D., F. d'Ortenzio, S. B. Hooker, G. Becu, B. Gentili, D. Tailliez, and A. J. Scott, 2008: Assessment of uncertainty in the ocean reflectance determined by three satellite ocean color sensors (MERIS, SeaWiFS and MODIS-A) at an off-shore site in the Mediterranean Sea (BOUSSOLE project). *J. Geophys. Res.*, **113**, C07013, doi:10.1029/2007JC004472.
- Barnes, R. A., R. E. Eplee Jr., G. M. Schmidt, F. S. Patt, and C. R. McClain, 2001: The calibration of SeaWiFS. 1. Direct techniques. *Appl. Opt.*, **40**, 6682–6700, doi:10.1364/AO.40.006682.
- Bartlett, J. S., K. J. Voss, S. Sathyendranath, and A. Vodacek, 1998: Raman scattering by pure water and seawater. *Appl. Opt.*, **37**, 3324–3332, doi:10.1364/AO.37.003324.
- Clark, D. K., H. R. Gordon, K. J. Voss, Y. Ge, W. Broenkow, and C. C. Trees, 1997: Validation of atmospheric corrections over oceans. *J. Geophys. Res.*, **102**, 17 209–17 217, doi:10.1029/96JD03345.
- , and Coauthors, 2003: MOBY, a radiometric buoy for performance monitoring and vicarious calibration of satellite ocean color sensors: Measurement and data analysis protocols. Special topics in ocean optics protocols and appendices, J. L. Mueller, G. S. Fargion, and C. R. McClain, Eds., Ocean optics protocols for satellite ocean color sensor validation, Revision 4, Vol. VI, NASA Tech. Memo. NASA/TM-2003-211621, 3–34. [Available online at https://oceancolor.gsfc.nasa.gov/docs/technical/protocols_ver4_volvi.pdf.]
- Donlon, C., and Coauthors, 2012: The Global Monitoring for Environment and Security (GMES) Sentinel-3 mission. *Remote Sens. Environ.*, **120**, 37–57, doi:10.1016/j.rse.2011.07.024.
- Eplee, R. E., Jr., W. D. Robinson, S. W. Bailey, D. K. Clark, P. J. Werdell, M. Wang, R. A. Barnes, and C. R. McClain, 2001: Calibration of SeaWiFS. II. Vicarious techniques. *Appl. Opt.*, **40**, 6701–6718, doi:10.1364/AO.40.006701.
- Franz, B. A., S. W. Bailey, P. J. Werdell, and C. R. McClain, 2007: Sensor-independent approach to the vicarious calibration of satellite ocean color radiometry. *Appl. Opt.*, **46**, 5068–5082, doi:10.1364/AO.46.005068.
- Ge, Y., K. J. Voss, and H. R. Gordon, 1995: In situ measurements of inelastic scattering in Monterey Bay using solar Fraunhofer lines. *J. Geophys. Res.*, **100**, 13 227–13 236, doi:10.1029/95JC00460.
- Gordon, H. R., 1979: Diffuse reflectance of the ocean: The theory of its augmentation by chlorophyll a fluorescence at 685 nm. *Appl. Opt.*, **18**, 1161–1166, doi:10.1364/AO.18.001161.
- , 1999: Contribution of Raman scattering to water-leaving radiance: A reexamination. *Appl. Opt.*, **38**, 3166–3174, doi:10.1364/AO.38.003166.
- , and K. Ding, 1992: Self-shading of in-water optical instruments. *Limnol. Oceanogr.*, **37**, 491–500, doi:10.4319/lo.1992.37.3.0491.
- JCGM, 2008: Evaluation of measurement data—Guide to the expression of uncertainty in measurement. Joint Committee for Guides in Metrology Doc. JCGM 100:2008, 120 pp. [Available online at http://www.bipm.org/utls/common/documents/jcgm/JCGM_100_2008_E.pdf.]
- Kiefer, D. A., 1973: Fluorescence properties of natural phytoplankton populations. *Mar. Biol.*, **22**, 263–269, doi:10.1007/BF00389180.
- Lee, Z. P., and C. Hu, 2006: Global distribution of Case-1 waters: An analysis from SeaWiFS measurements. *Remote Sens. Environ.*, **101**, 270–276, doi:10.1016/j.rse.2005.11.008.
- Li, L., D. Stramski, and R. A. Reynolds, 2016: Effects of inelastic radiative processes on the determination of water-leaving spectral radiance from extrapolation of underwater near-surface measurements. *Appl. Opt.*, **55**, 7050–7067, doi:10.1364/AO.55.007050.
- Mobley, C. D., and Coauthors, 1993: Comparison of numerical models for computing underwater light fields. *Appl. Opt.*, **32**, 7484–7504, doi:10.1364/AO.32.007484.
- Morel, A., and L. Prieur, 1977: Analysis of variations in ocean color. *Limnol. Oceanogr.*, **22**, 709–722, doi:10.4319/lo.1977.22.4.0709.
- , D. Antoine, and B. Gentili, 2002: Bidirectional reflectance of oceanic waters: Accounting for Raman emission and varying particle scattering phase function. *Appl. Opt.*, **41**, 6289–6306, doi:10.1364/AO.41.006289.
- Mueller, J. L., 2004: Shadow corrections to in-water upwelled radiance measurements: A status review. Special topics in ocean optics protocols, part 2, J. L. Mueller, G. S. Fargion, and Charles R. McClain, Eds., Ocean optics protocols for satellite ocean color sensor validation, Revision 5, Vol. VI, NASA Tech. Memo. NASA/TM-2004, 1–7. [Available online at https://oceancolor.gsfc.nasa.gov/docs/technical/protocols_ver5_volvi_pt2.pdf.]
- Sugihara, S., M. Kishino, and M. Okami, 1984: Contribution of Raman scattering to upward irradiance in the sea. *J. Oceanogr. Soc. Japan*, **40**, 397–404, doi:10.1007/BF02303065.
- Wang, M., X. Liu, L. Tan, L. Jiang, S. H. Son, W. Shi, K. Rausch, and K. Voss, 2013: Impacts of VIIRS SDR performance on ocean color products. *J. Geophys. Res. Atmos.*, **118**, 10 347–10 360, doi:10.1002/jgrd.50793.
- Yarbrough, M. A., and Coauthors, 2007a: Results in coastal waters with high resolution in-situ spectral radiometry: The Marine Optical System ROV. *Coastal Ocean Remote Sensing*, R. J. Frouin, Ed., International Society for Optical Engineering (SPIE Proceedings, Vol. 6680), 66800I, doi:10.1117/12.735064.
- , and Coauthors, 2007b: Simultaneous measurement of upwelling spectral radiance using a fiber-coupled CCD spectrograph. *Coastal Ocean Remote Sensing*, R. J. Frouin, Ed., International Society for Optical Engineering (SPIE Proceedings, Vol. 6680), 66800J, doi:10.1117/12.735016.
- Zibordi, G., J.-F. Berthon, F. Mélin, and D. D'Alimonte, 2011: Cross-site consistent in situ measurements for satellite ocean color applications: The BiOMaP radiometric dataset. *Remote Sens. Environ.*, **115**, 2104–2115, doi:10.1016/j.rse.2011.04.013.